PCCP

PAPER

Controlling the off-center positions of anions through thermodynamics and kinetics in flexible perovskite-like materials†

Cite this: DOI: 10.1039/d0cp05711h

A. Lobato, * M. Recio-Poo, A. Otero-de-la-Roza, M. A. Salvadó and J. M. Recio *

Received 2nd November 2020,
Accepted 16th December 2020

DOI: 10.1039/d0cp05711h

rsc.li/pccp

Due to the network flexibility of their BX_3 sub-lattice, a manifold of polymorphs with potential multiferroic applications can be found in perovskite-like ABX_3 materials under different pressure and temperature conditions. The potential energy surface of these compounds usually presents equivalent off-center positions of anions connected by low energetic barriers. This feature facilitates a competition between the thermodynamic and kinetic control of the transitions from low to high symmetry structures, and explains the relationship between the rich polymorphism and network flexibility. In the rhombohedral phase of iron trifluoride, our first-principles electronic structure and phonon calculations reveal the factors that determine which of the two scenarios dominates the transition. At the experimentally reported rhombohedral–cubic transition temperature, the calculated fluorine displacements are fast enough to overcome a forward and backward barrier of less than 30 kJ mol^{-1}, leading to an average structure with cubic symmetry. In addition, lattice strain effects observed in epitaxial growth and nanocrystallite experiments involving BX_3 compounds are successfully mimicked by computing the phase stability of FeF_3 under negative pressures. We predict a transition pressure at −1.8 GPa with a relative volume change around 5%, consistent with a first-order transition from the rhombohedral to the cubic structure. Overall, our study illustrates how, by strain tuning, either a thermodynamic or a kinetic pathway can be selected for this transformation.

1. Introduction

Aristotype cubic polymorphs emerging at increasing temperatures are of broad interest in diverse fields such as materials science,[1] planetology[2] or solid-state chemistry[3] and physics.[4] The properties of these high symmetric phases are often related to a phenomenon called network flexibility (NF).[5,6] Along temperature-induced phase transitions, the material, instead of behaving as a rigid body, experiences subtle local structural changes involving on- and off-center positions of anions.[7] These changes are associated with revertible atomic movements connecting at least two equivalent lattice configurations that can be identified with double- or multiple-wells on the potential energy surface (PES)[7–9] of the compound. The crystal family of ABX_3 halide perovskites is probably the most representative example of NF behavior.[1] Corner sharing BX_6 octahedra in these perovskites act as a flexible framework displaying polyhedral rotations (see Fig. 1), the amplitudes of which depend on the available thermal energy. It is the BX_3 sublattice that is mainly responsible for the rich polymorphism of ABX_3 crystals which, besides the archetypical aristotype ReO_3-type cubic structure, exhibits a variety of other lower symmetric hettotype phases modulated by the presence of the A cation.[10] This peculiar NF phenomenon causes the well-known multiferroic behavior in many perovskite materials, and is also the

MALTA Team and Departamento de Química Física y Analítica, Universidad de Oviedo, E-33006 Oviedo, Spain. E-mail: a.lobato@ucm.es, jmrecio@uniovi.es

† Electronic supplementary information (ESI) available. See DOI: 10.1039/d0cp05711h

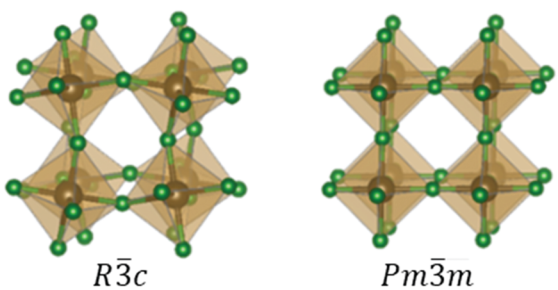

Fig. 1 Polyhedral view of the $R\bar{3}c$ α-FeF_3 and $Pm\bar{3}m$ ReO_3-type structures of FeF_3, the prototype BX_3 sublattice studied in this work. Green and brown balls stand for F and Fe atoms, respectively.

origin of other interesting properties such as zero thermal expansion[11,12] or anomalous Poisson ratios,[13] that allow these materials to be applied as field-effect transistors,[14,15] photovoltaics[16–18] or high-performance magnets.[19]

However, in spite of ReO_3-type materials being promising, the mechanisms that enable the apparition of the symmetric cubic phase are still unclear. On one hand, X-ray, Raman and calorimetric analyses of BF_3 (B = Al, Cr, Ga, V and Fe) compounds at different temperatures pointed towards the phase transition of a weak first-order type.[20] In contrast, analysis of pair distribution function data from real time measurements has displayed a completely different view of the formation of the cubic phase in AlF_3:[21] This appears as a consequence of the quick interconversion between two equivalent rhombohedral phases. These structures are distortions of the cubic phase and are stable at lower temperatures. Interestingly, the latter view agrees with the computational vibrational studies on $RbCaF_3$[22] and $CsPbI_3$[23–25] perovskites, in which the presence of soft phonons in the cubic phase evidences an order–disorder interconversion between the minima of the anharmonic double-well potentials. Moreover, it seems that regardless of the organic or inorganic nature of the central cation,[26] the temperature-induced formation of the cubic phase in perovskites is also produced by the dynamic disorder of the structure, highlighting that the conditions for the formation of the high symmetry phase in these materials also include the nature of the BX_3 sublattices. This is a clear illustration of the competition between thermodynamics and kinetics in materials synthesis.[27]

Lattice strain effects during nanoparticle formation[28,29] and epitaxial growth experiments[30,31] in BX_3 and ABX_3 materials can also induce the formation of the cubic phase. In these cases, first order phase transitions are reported, suggesting a different mechanism for the formation of the highly symmetric aristotype cubic phase. In order to explain these observations, the influence of tensile effects or negative pressure on phase stability must be considered.

In this work, we reveal the impact of lattice strains induced by temperature and negative pressure on the phase stability of FeF_3, a prototypical material displaying network flexibility. The first- and second-order phase transition types are discussed using density functional theory (DFT) calculations. Kinetic effects will be also included in our discussion since the comparison between the time-scale of the experiments and the phase interconversion may offer information about the nature of the phase transition.[32] The possibility of non-equilibrium metastable structures will be explicitly considered.[27] In fact, our results show how the temperature-induced formation of the cubic phase must be seen as dominated by a kinetic mechanism, highlighting the importance of considering a dynamic picture in double well phenomena and the possibility of metastability in dynamic unstable lattices.[4] In contrast, but not incompatible, negative pressures are shown to induce the stabilization of the highly symmetric cubic structure by means of a first order-type phase transition, in agreement with observations from epitaxial growth and nanoparticle experiments.

Our results are expected to provide insights on different families of halide perovskites. Indeed, according to the tolerance factor parameter in ABX_3 perovskites introduced by Goldschmidt (quoted for example in ref. 25), values between 0.9 and 1 results in a cubic structure, whereas values between 0.71 and 0.9 are found for the rhombohedral/orthorhombic structures. Based on this pure ionic bonding criteria, ABF_3 perovskites with A monopositive cations displaying radii between 0.66 and 1.17 Å and B radius similar to Fe^{3+} (0.65 Å) are expected candidates to present similar effects as those we will discuss in the FeF_3 system. Moreover, the spherical nature of the s-type orbitals of the divalent B cations in ABX_3 halide perovskites allows an overlapping with the p-type orbitals of the halogens at different X–B–X angles,[33] similar to that produced by the interaction with d-type orbitals in the case of transitions metals, as in our FeF_3 crystal. Since the lattice flexibility is related to the strength of the metal–halogen bond, these common B–X bonding characteristics indicate that the conclusion from our investigation could be applied to understand the formation mechanism of the cubic phase in other ABX_3 halide perovskites, such as in $CsPbI_3$, $CsSnF_3$, $CsSnBr_3$ or $CsGeBr_3$. It is noteworthy that, in analogy with our FeF_3 results below, $CsPbI_3$ has shown to present a kinetically stabilized cubic phase.[23–25]

2. Computational details

In the rhombohedral setting, the unit cell of the $R\bar{3}c$ α-FeF_3 phase is characterized by a unit cell parameter, a cell angle, and the x coordinate of the F crystallographic position ($-x_F$, 1/2 − x_F,1/4), being Fe atoms at (0,0,0). When x_F = 0.25 and the cell angle is 60°, the rhombohedral phase collapses into the cubic $Pm\bar{3}m$ ReO_3-type structure (see Fig. 1 and ESI†).

The PES as a function of the rhombohedral unit cell volume (V) and fluorine crystallographic position of FeF_3 (x_F) was calculated in a grid of 11 × 10 (V, x_F) points using density functional theory formalism with the plane-wave pseudopotential scheme implemented in Quantum ESPRESSO (QE).[34] The projector augmented wave (PAW) method was used,[35] and the B86bPBE functional for the exchange–correlation contribution[36] was chosen. $3d^64s^2$ and $2p^5$ electrons have been considered as valence electrons for Fe and F, respectively. A Hubbard-like energy term was included with a U parameter of 5 eV in order to treat the strong on-site Coulomb interaction of the d-electrons in iron,[37] similar to the GGA+U calculations of Li *et al.* in the α phase.[38] The exchange-hole dipole moment[39,40] (XDM) model for van der Waals weak interactions has also been used with the canonical damping function parameters (a_1 = 0.6512 and a_2 = 1.4633 Å). A plane-wave kinetic energy cutoff of 70 Hartree ensures a convergence in the energy in the order of 10^{-5} Hartree and 0.5 GPa in the stress tensor.

Since Fe is an open shell atom and FeF_3 displays an antiferromagnetic behaviour under room conditions (the Néel temperature of the rhombohedral phase is 365 K[41]), spin-polarized calculations were carried out. Using the rhombohedral setting for the cubic structure, both the low- and high-symmetry structures were found to contain two Fe^{3+} in the unit cell. Thus, in order to simulate the antiferromagnetic (AFM) ordering, we select one Fe^{3+} ion with all its five open shell

electrons being alpha, whereas all the open shell electrons of the second Fe^{3+} are beta. Geometry optimizations are carried out using these spin polarized orderings. We repeated the calculations considering that the electrons of the two Fe^{3+} ions in the corresponding unit cells are all alpha (or beta) (FM state) and compared the energies with the AFM calculations at different volumes. Differences in energies and structural parameters are lower than 5×10^{-3} Hartree and 0.01 Å. When these results are translated to the calculated PES, we observe that our conclusions are not meaningful, affected by the specific magnetic ordering of the two phases since the order of magnitude of the magnetic energy contribution is much smaller than the energies involved in the structural transformations. On the other hand, the description of FeF_3 as non-magnetic (non-spin-polarized calculations) yields unrealistic $E(V)$ curves, with differences with respect to AFM and FM orderings as high as 0.1 Hartree. To take into account vibrational (thermal) effects under the so-called quasiharmonic approximation (QHA),[42] evaluation of phonon dispersion curves for the α and ReO_3-type phases was carried out within the DFPT perturbation scheme[42] implemented in QE. These calculations were performed at the relaxed equilibrium geometries (maximum forces on atoms are lower than 10^{-4} Hartree $Bohr^{-1}$) obtained at the same volumes where the total energy was minimized. A grid of $2 \times 2 \times 2$ vibrational **q** wavevectors was sampled in the first Brillouin zone. Gibbs2 code[43,44] was used to describe the computed (E,V) points of the two FeF_3 phases by means of numerical and analytical equations of state (EOS). Specifically, the code allows one to determine the Vinet[45] isothermal EOS parameters (volume, V_0; bulk modulus, B_0; and its pressure derivative, B_0'; all evaluated at zero pressure) at static and temperatures up to 1350 K.

3. Results

3.1 Flexible behavior and double well phenomena in BX3 sublattices

Four-membered octahedral rings are the units of the rhombohedral and cubic phases of FeF_3. Halide atoms act as hinges connecting the octahedral building blocks centered at iron atoms. These FeF_6 octahedra can rotate easily under external stimuli,[46] while the general shape and the Fe–F nearest neighbor distances are preserved following the so-called rigid unit model.[47] The Fe–F–Fe angle can be used to parametrize the relative motion of the octahedra, with 180° degrees corresponding to the cubic structure. In Fig. 2, we show the PES of the rhombohedral FeF_3 as a function of the unit cell volume and the crystallographic (internal) coordinate of the F atom. The aristotype cubic phase is located along the $x_F = 0.25$ centreline of the plot, corresponding to a ridge in the PES at small volumes. The hettotype rhombohedral phases are located in the symmetrical basins above and below this centreline, with energy minima at $x_F = 0.126$ and $x_F = 0.374$ at the calculated equilibrium static volume $V = 51.1$ Å^3 (see black dots in Fig. 2 right). This picture shows the existence of two equivalent atomic configurations at both sides of the highly symmetric cubic phase, the neccessary ingredients for a material to present NF. Notice that a one dimensional energetic profile with a double well shape appears when we select a slice of this PES at any constant volume below 60 Å^3. This feature is common to other BX_3 sublattices of ABX_3 halide perovskites.[23,25,48,49] Thus, the discussion can be of interest to this crystal family since the central A cation of a particular ABX_3 perovskite structure does not hinder the formation of the two equivalent configurations. We study the emergence of the high symmetry cubic phase followed by both a thermodynamic displacive and a kinetic perspective of this transformation. First, the high-volume region of the PES, where the cubic phase shows the lowest energy, can be sampled by increasing the temperature of the system, which induces positive (expansion) lattice strains. The same effect can be achieved by applying negative pressures, such as those found during epitaxial growth experiments. The comparison of the energetics of the two phases under these conditions lead to a thermodynamic view of the transformation from the rhombohedral to the cubic structure. Secondly, the low barrier connecting the valleys at a given volume (see Fig. 2 (left)), and its decreasing height as volume increases, can metastabilize the cubic phase due to a kinetic mechanism or

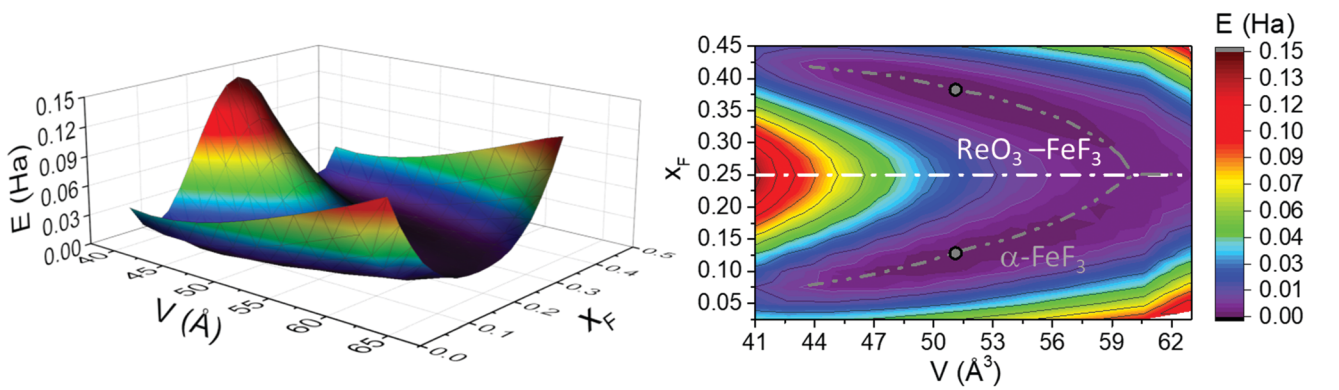

Fig. 2 Left: Potential energy surface as a function of volume per formula unit (V) and fluorine crystallographic position (x_F) in the rhombohedral unit cell of FeF_3. Right: 2D contour diagram of the FeF_3 potential energy surface, white and grey dash dotted lines stand for the ReO_3–FeF_3 and the α-FeF_3 energy–volume equation of states, respectively. The two equivalent rhombohedral equilibrium structures under static conditions are denoted with dots.

equivalently through dynamic disorder effects. At moderate temperature, before reaching the region where the cubic phase shows the lowest energy, the system can overcome the barrier backwards and forwards and delocalize between the two equivalent rhombohedral phases. The challenge is to disclose under which conditions the transition from the hettotype low-symmetry phase to the aristotype high-symmetry phase is kinetically or thermodynamically driven, and if this is the case, whether it is of a first- or a second-order type.

3.2 Temperature-induced phase transition: order–disorder jumping between wells

Our energy–volume curve shows that the α-phase of FeF_3 evolves continuously from its equilibrium structure calculated at V = 51.1 Å^3 (51.9 Å^3 is the experimental value under room conditions[50]) towards the cubic phase, as illustrated in Fig. 3a by the decrease in the height of the arrows connecting both phases. Moreover, as expected from the PES, the cubic structure displays imaginary phonon frequencies up to the volume at which both structures merge (∼60 Å^3) evidencing that it is dynamically unstable in this volume range (51–60 Å^3) because it corresponds to an energy maximum in the configurational space (see Fig. 3b). Experimentally, a cubic FeF_3 polymorph was firstly observed by Croft and Kestigian[51] at 683 ± 5 K, a temperature a little bit higher that the value reported by Daniel *et al.*[20] (654 ± 7 K), who concluded that FeF_3 transforms into the cubic phase through a temperature induced first-order phase transition. However, a low transition enthalpy (less than 1 kJ mol^{-1}) and a small hysteresis range of 15 K also accompany this transformation. In Fig. 4, we present the V–T equation of the state of α-FeF_3 evaluated after phonon dispersion calculations under the quasi-harmonic approximation.

It shows good agreement with the available experimental data in the 80–400 K range.[41]

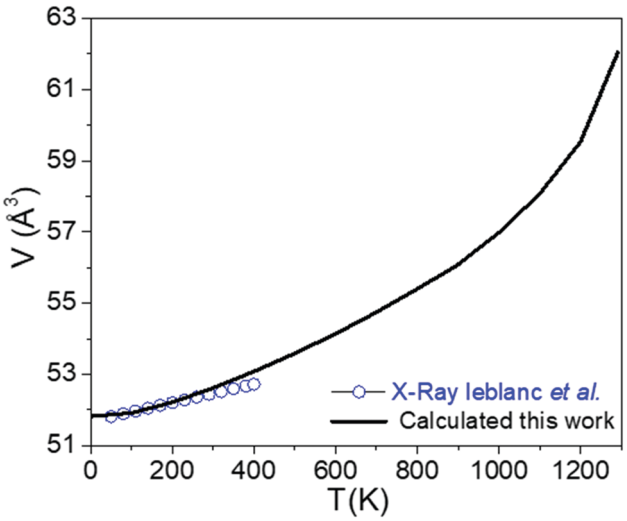

Fig. 4 Calculated V–T equation of state for α-FeF_3 (black empty dots) along with the available experimental V–T data from X-ray measurements[41] in the range of 80–400 K.

Since the reported transition temperatures correspond to volumes within the range where the cubic phase is dynamically unstable, we conclude that our results are not compatible with a temperature-induced first order phase transition in FeF_3. Rather, our results would suggest a second order phase transition where the low-symmetry phase would approach continuously to the higher symmetry ReO_3-type phase as volume increases. To check the plausibility of this temperature-induced second order phase transition, we have carried out an analysis of the PES using the Landau formalism.

According to the symmetry restrictions provided by the Landau theory, the energy of the ReO_3–FeF_3 ($Pm\bar{3}m$) to α-FeF_3 ($R\bar{3}c$) transition is characterized using a six-order potential of the formula:[52]

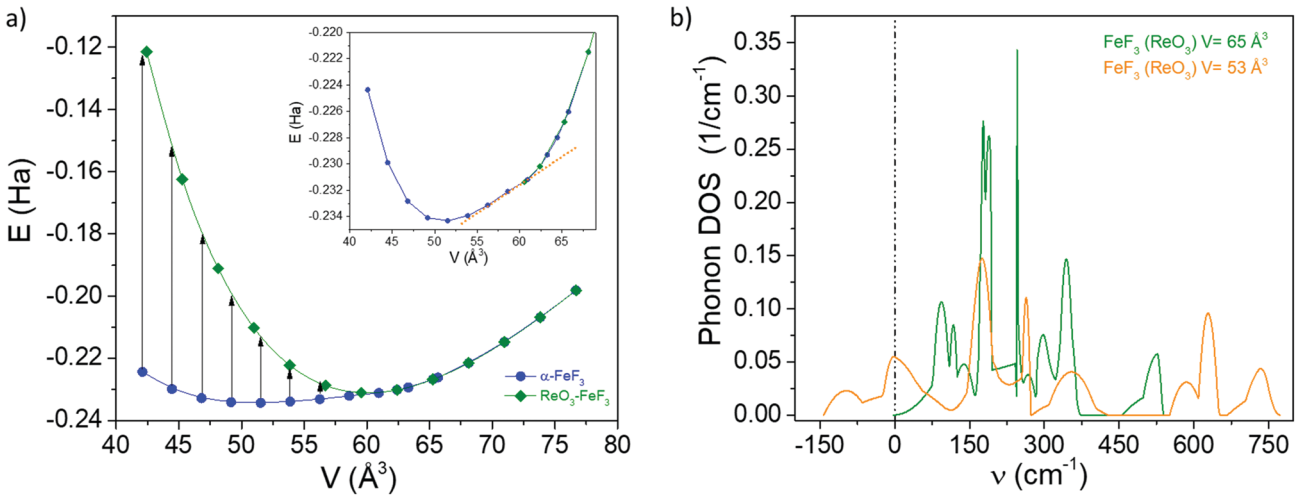

Fig. 3 (a) Energy–volume equation of state for the α-FeF_3 (blue dots) and ReO_3-type FeF_3 (green diamonds) structures. The inset displays a zoom view of the volume range where a common tangent is plotted. (b) Phonon energy density of states for the ReO_3-type FeF_3 at unit cell volumes of 53 Å^3 (orange) and 65 Å^3 (green).

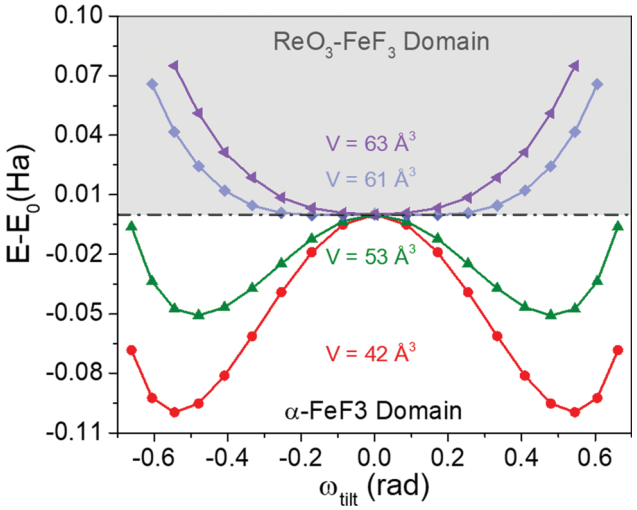

Fig. 5 1D-energy potentials obtained from the PES at 42 Å^3 (red circles), 53 Å^3 (green triangles), 61 Å^3 (light blue squares) and 63 Å^3 (purple triangles). The energy of the ReO_3 structure has been taken as the reference zero of energy. Grey and white regions define the stability domains of the ReO_3-type and the α structures, respectively.

$$E - E_0 = A(T - T_c)^{1/2}\omega_{tilt}^{\ 2} + B\omega_{tilt}^{\ 4} + C\omega_{tilt}^{\ 6} \quad (1)$$

where E_0 is the reference energy, A, B and C are polynomial expansion coefficients, T_c is the critical temperature, the temperature at which the E–ω_{tilt} curve changes from a maximum to a minimum at $\omega_{tilt} = 0$, and ω_{tilt} is the order parameter, which in this case corresponds to the octahedral tilting angle. The latter can be readily determined from the fluorine crystallographic position (x_F) using the expression:

$$\tan(\omega_{tilt}) = \sqrt{3}(1 - 2x_F) \quad (2)$$

In Fig. 5, we show 1D-energy potentials obtained from the PES as a function of the tilting angle, below and above the $Pm\bar{3}m$ ($\omega_{tilt} = 0$) structure, at four different fixed volumes. The energy of the cubic structure at each volume has been taken as a zero-energy reference. The curves at volumes greater than 60 Å^3 display only one minimum showing the stability of the ReO_3 structure in this domain, whereas at lower volumes the α-FeF_3 domain is characterized with double well potentials. Across all the volumes studied, our fitting results show negligible odd terms (less than 10^{-10}) as well as values for the quartic term greater than zero, both clear signatures compatible with a second order nature for this transformation.[52,53] The non-negligible quartic and six-order parameters in the Landau free energy evidence the highly anharmonic behaviour expected for a flexible and mechanically soft lattice.[32] Indeed, our phonon analysis as a function of the unit cell volume reveals two soft optical modes with frequencies of 120 (E_g) and 190 (A_{1g}) cm^{-1} at the static equilibrium volume of α-FeF_3 (see Fig. 6 left), in fair agreement with the values of 94 (E_g) and 168 (A_{1g}) cm^{-1} reported by Daniel *et al.* under room conditions.[20]

These soft modes are associated with the octahedral rotational movements that allow the lattice to move from the α-FeF_3 to the ReO_3-type structure. The soft nature of these modes is further confirmed by the phonon analysis of the cubic phase. The group–subgroup relationship between the $Pm\bar{3}m$ and the $R\bar{3}c$ phases is accompanied by the condensation of the E_g and A_{1g} modes into one triple degenerated mode in the R point of the Brillouin zone of the cubic structure.[54] Our results show a triple degenerated imaginary mode (R_5) in the cubic phase which becomes zero around 60 Å^3, revealing that the dynamic instability of the cubic phase disappears at this volume. This is just the same volume at which static E–V curves of α and ReO_3 phases converge (see Fig. 3a).

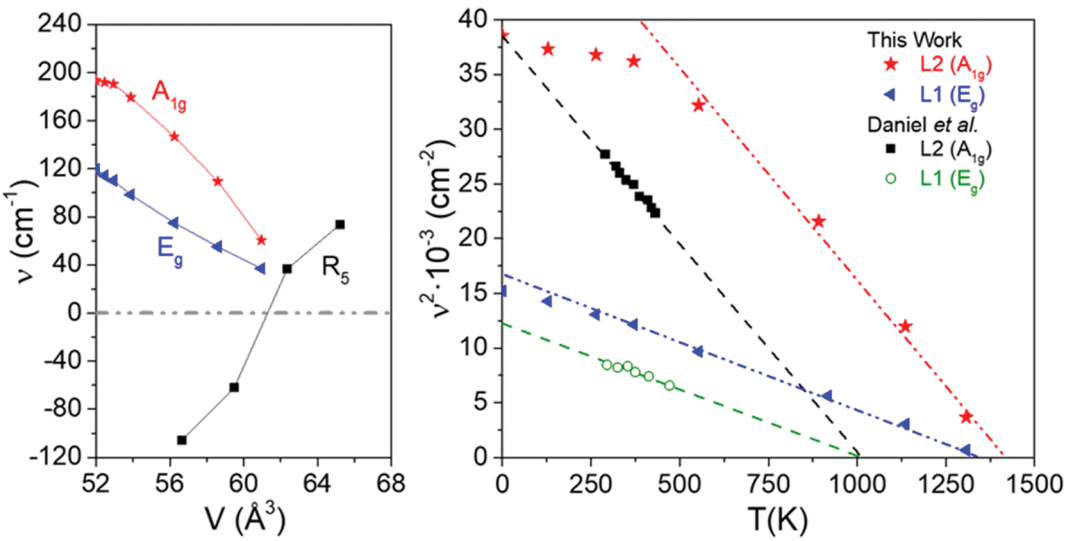

Fig. 6 (left) Volume dependence of the soft A_{1g} (red stars) and E_g (blue triangles) vibrational modes in the α-FeF_3 phase. Black squares correspond to the triple degenerate R_5 mode of the ReO_3–FeF_3 structures. Negative frequency values stand for the imaginary contributions of this mode at volumes lower than 61 Å^3. (Right) Calculated temperature dependence of the A_{1g} (red stars) and E_g (blue triangles) modes. Green empty circles and black squares are the experimental data provided by Daniel *et al.* for the A_{1g} and E_g modes, respectively.

We have used our computed V–T EOS to associate temperatures with the corresponding volumes at which the soft phonon frequencies were calculated. Fig. 6 (right) displays the temperature dependence of the square frequencies of these E_g and A_{1g} soft phonons. Our results for both modes perfectly follow the classical Landau dependence on high temperature,[36] showing a linear decrease at values higher than 300 K. Compared with Raman experimental data, also included in Fig. 6 (right), our frequencies are less than 25 cm^{-1} blue-shifted and show similar temperature slopes. This result supports our PES + QHA approach. The extrapolated value at which the two soft modes condense provides a T_c calculated value of 1350 K, whereas the experimental reported value for T_c is 1013 K.[20] These values are much higher than the observed transition temperature between 683 K and 654 K reported, respectively, by Croft and Kestigian[51] and by Daniel *et al.*[20] The discrepancy between the critical temperatures and the experimental observations lead us to rule out a second-order thermodynamic perspective to explain the transformation. At this point, it is appealing to resort to a kinetic view as the responsible mechanism for the formation of the cubic phase. Interestingly, the low frequency E_g and A_{1g} soft modes can be easily activated by increasing the temperature leading to large fluorine displacements.

If the available thermal energy at a given temperature was enough to overcome the barrier, then a rapid interchange between both rhombohedral structures could lead to the observation of the average structure, namely the cubic phase. The emergence of the high symmetry structure in FeF_3 would be thus achieved through a dynamic disorder process.

A quantitative analysis of the dynamic disorder in FeF_3 can be provided by estimating the transformation rate (Γ) or equivalently the interconversion time (τ) between the two equivalent minima of the double well potential. Using a classical Arrhenius model, the latter quantities are expressed as:

$$\Gamma = \frac{1}{\tau} = \nu_a e^{-\frac{E_b}{k_B T}} \quad (3)$$

where E_b and ν_a are the energy difference between the ReO_3-type and α structures at the same volume and the classical attempt frequency, respectively. ν_a is easily calculated from the second derivative of the E–ω_{tilt} function (see eqn (1)) as detailed in the ESI.†

Eqn (3) provides a straightforward procedure to estimate the temperature at which the available thermal energy is enough to produce a fast interconversion between the two equivalent minima of the structure. Previous studies applied this equation considering the barrier energy at a particular volume and evaluated the available energy at different temperatures.[23,25] As revealed by our PES analysis, barrier energy, volume and temperature are not independent variables. For instance, at 306 K, the volume provided by our computed V–T EOS is 52.5 $Å^3$ and the energy barrier is 46.4 kJ mol^{-1}, whereas at a higher temperature (1036 K), the volume increases to 56.2 $Å^3$ and the barrier decreases to 14.3 kJ mol^{-1}. Here, the evaluation of the transformation rate and the interconversion time at a given volume is performed using the energy barrier and the temperature determined using the PES and the V–T EOS, respectively. Our results are summarized in Table 1. In order to propose an estimation of the temperature at which the cubic structure is observed, it is necessary to consider the time-scale of the experiments. Molecular dynamics simulations coupled to UV-visible spectroscopic measurements in organic halide perovskites provide a reasonable criterion.[32,55] These results have shown that a statistical average population of a cubic phase is obtained when dynamic fluctuations occur in scales of tens of picoseconds. Our calculations (see Table 1) show that only above 663 K the interconversion times (41.8 ps) are high enough to fulfil the time scale requirement of more than tens of picoseconds. Accordingly, the kinetic model estimates a temperature around 663 K for the emergence of the cubic structure, in close agreement with the observed transition temperature range of 646–661 K reported in ref. 20 and 51.

Table 1 Calculated parameters of eqn (3) at selected volumes. V, T, E_b, ν_a, Γ, and τ stand for the volume, temperature, barrier energy, attempt frequency, transformation rate and interconversion time, respectively

V ($Å^3$)	T (K)	E_b (kJ mol^{-1})	ν_a (cm^{-1})	Γ (s^{-1})	τ (s)
52.47	263	46.42	153.0	2.65×10^{3}	3.77×10^{-4}
52.94	370	41.04	150.3	6.84×10^{6}	1.46×10^{-7}
53.88	553	30.46	138.9	1.38×10^{10}	1.86×10^{-10}
54.53	663	24.40	131.2	4.62×10^{10}	4.18×10^{-11}
55.22	771	19.69	123.0	1.69×10^{11}	1.15×10^{-11}
56.24	917	14.28	110.9	5.06×10^{11}	1.97×10^{-12}
58.60	1135	4.71	82.2	1.49×10^{12}	6.69×10^{-13}

The existence of a metastable phase linked to a dynamically unstable structure[4] is an interesting corollary from our kinetic study. It is the network flexibility of the BX_3 lattice which produces a highly anharmonic double well surface. When thermal effects come into play, the kinetic control precedes the transition and prevents a potential second order phase transition at a higher temperature. Specifically, BF_3 (B = Al, Cr, Ga, V and Fe) compounds should behave similarly with kinetically controlled transformations at calculated temperatures close to the ones reported in ref. 20 (between 650 K and 775 K for AlF_3, VF_3, and FeF_3, and between 1100K and 1250 K for GaF_3 and CrF_3). There is not a clear relationship between temperature and cation radius of these compounds, although in all cases the rhombohedral structure at room temperature is expected for BF_3 crystals with $r(B^{3+})$ between 0.5 and 0.8 Å.

3.3 Thermodynamic control of the transition through negative pressures

Previous studies on halide perovskites and BX_3 perovskite-defective materials have evidenced the existence of a cubic phase in epitaxial growth experiments[30,31] at a nanocrystal scale.[28,29] Under these conditions, the mechanism responsible for the α to the cubic transformation is still unclear. Yang *et al.*[25] quoted that, rather than surface effects, lattice strain or phonon confinement, it is dynamic disorder[56] that is mainly responsible for this transformation in caesium lead halide perovskites. Interatomic distances greater than those at

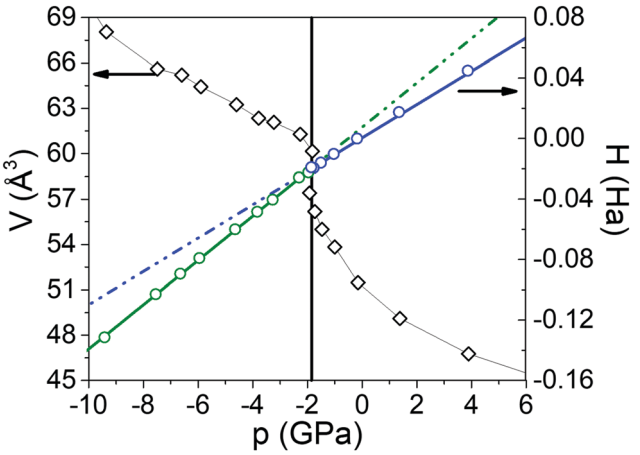

Fig. 7 Pressure dependence of volume (empty black diamonds) and enthalpy (green and blue circles) for the rhombohedral FeF_3 structure. Dashed-dotted lines represent an extrapolation of the linear trend displayed by the enthalpy of the two phases in their corresponding stability regimes.

equilibrium configurations appear in the structures during the epitaxial growth and nanoparticle formation experiments and can be recreated by introducing tensile forces or negative stresses in computational simulations.

The calculated E–V curves allow us to study the relative stability of the α and ReO_3-type structures at negative pressures. A striking feature in the α curve appears around 58.5 Å^3 (see the inset in Fig. 3a). Our computational analysis of this curvature change confirms that it corresponds to two consecutive inflexion points. Since the former occurs at a lower volume than that of the merging point (~60 Å^3), a common tangent line can be drawn connecting the α and the cubic phases. This fact reveals that under negative pressures the transformation from the α to the cubic structure has a first order character. To quantitatively evaluate the transition pressure (p_t) and volume change during transition (ΔV_t), we have numerically calculated the enthalpy as a function of pressure in the volume ranges where the α (48–60 Å^3) and the cubic (61–69 Å^3) phases are dynamically stable (see Fig. 7). We observe a subtle slope change at $p_t = -1.8$ GPa defining the transition pressure. At this pressure, the unit cell volume also suffers a sudden volume change ($\Delta V_t \sim 3$ Å^3). These results confirm the thermodynamic nature of the transition in the negative pressure regime in the absence of thermal effects. On increasing the temperature, the α to the cubic transformation could be observed at slightly lower negative pressures ($P_t > -1.8$ GPa). The success of our calculations in predicting the appearance of a stable FeF_3 cubic phase under negatives pressures reveals the crucial role of lattice strains that could be generalized to analyse the phase stability of other BX_3 sub-lattices.

4. Conclusions

Using the potential energy surface of FeF_3 as a prototype for other perovskite BX_3 rhombohedral sublattices, we have shown that the interesting high symmetry aristotype cubic phase is clearly located along the ridge separating two equivalent basins where the hettotype α phase resides. Based on the features of the surface, we have shown that anharmonicity and double well phenomena are associated with the network flexibility of FeF_3. It is worth highlighting the diametrically different views provided by our simulations on the effects of temperature and (negative) pressure. The former describes a kinetically controlled transition, preventing a second order scenario. Using a simple kinetic model, we obtained a fast-enough interconversion rate at temperatures very similar to those where the α to cubic transformation in FeF_3 was observed. This temperature around 680 K is well below the critical temperatures derived from the second order Landau analysis using both computational (~1350 K) and experimental (~1000 K) data. As FeF_3 represents a common BX_3 sublattice, the observed transitions induced by dynamic disorder in halide perovskites can be understood by resorting to these results. Conversely, negative pressure allows a thermodynamic stabilization of the cubic phase in accordance with a first order character for the transformation from the α to the cubic phase in FeF_3. This result is compatible with the observed preference of high symmetry phases in halide perovskites during nanoparticle and epitaxial growth experiments.

We believe that the results shown here can be potentially used to develop new crystal engineering strategies directed towards the stabilization of specific structures in halide perovskite-like materials. Specifically, phase transitions in ABF_3 perovskites, with A monopositive cations displaying radii between 0.66 and 1.17 Å and B radius similar to Fe^{3+} (0.65 Å), and ABX_3 halide perovskites where B is a divalent cation such as $CsPbI_3$, $CsSnF_3$ and $CsSnBr_3$, could be explained using our thermodynamic and kinetic perspective due to the flexible characteristics produced by the metal–halogen bonds. Our results reveal that combining pressure and temperature, we can modulate strains in BX_3 sublattices and (dis)favor the kinetic/thermodynamic control of the transformation. If only temperature is increased, both the kinetic and thermodynamic control of the transition are favoured, and hence dynamic disorder increases, which induces more positive strains in the lattice.

Conflicts of interest

There are no conflicts to declare.

Acknowledgements

This work was supported by Ministerio de Ciencia e Innovación and Agencia Estatal de Investigación through the following projects: PGC2018-094814-B-C2, PGC2018-097520-A-100, RyC-2016-20301, and RED2018-102612-T. Funding was also provided by FICYT-Principado de Asturias (Spain) under Project No. FC-GRUPIN-IDI/2018/000177. MALTA Consolider

supercomputing center is gratefully acknowledged. We acknowledge David Abbasi (Silico Studio) for designing the TOC figure.

Notes and references

1 H. A. Evans, Y. Wu, R. Seshadri and A. K. Cheetham, *Nat. Rev. Mater.*, 2020, **5**, 196–213.

2 R. J. Hemley and R. E. Cohen, *Annu. Rev. Earth Planet Sci.*, 1992, **20**, 553–600.

3 J.-C. Bunzli and V. Pecharsky, *Handbook on the Physics and Chemistry of Rare Earths*, Elsevier Science B.V., 2009.

4 S. Kadkhodaei, Q.-J. Hong and A. van de Walle, *Phys. Rev. B*, 2017, **95**, 064101.

5 G. Férey and C. Serre, *Chem. Soc. Rev.*, 2009, **38**, 1380–1399.

6 N. Khosrovani and A. W. Sleight, *J. Solid State Chem.*, 1996, **121**, 2–11.

7 C. Katan, A. D. Mohite and J. Even, *Nat. Mater.*, 2018, **17**, 377–379.

8 A. Marronnier, G. Roma, S. Boyer-Richard, L. Pedesseau, J.-M. Jancu, Y. Bonnassieux, C. Katan, C. C. Stoumpos, M. G. Kanatzidis and J. Even, *ACS Nano*, 2018, **12**, 3477–3486.

9 P. Acharyya, T. Ghosh, K. Pal, K. Kundu, K. Singh Rana, J. Pandey, A. Soni, U. V. Waghmare and K. Biswas, *J. Am. Chem. Soc.*, 2020, **142**, 15595–15603.

10 P. Woodward, *Acta Crystallogr., Sect. B: Struct. Sci.*, 1997, **53**, 44–66.

11 J. Chen, X. Xing, C. Sun, P. Hu, R. Yu, X. Wang and L. Li, *J. Am. Chem. Soc.*, 2008, **130**, 1144–1145.

12 J. Chen, L. Hu, J. Deng and X. Xing, *Chem. Soc. Rev.*, 2015, **44**, 3522–3567.

13 C. W. Huang, W. Ren, V. C. Nguyen, Z. Chen, J. Wang, T. Sritharan and L. Chen, *Adv. Mater.*, 2012, **24**, 4170–4174.

14 S. P. Senanayak, M. Abdi-Jalebi, V. S. Kamboj, R. Carey, R. Shivanna, T. Tian, G. Schweicher, J. Wang, N. Giesbrecht, D. Di Nuzzo, H. E. Beere, P. Docampo, D. A. Ritchie, D. Fairen-Jimenez, R. H. Friend and H. Sirringhaus, *Sci. Adv.*, 2020, **6**, eaaz4948.

15 W. Yu, F. Li, L. Yu, M. R. Niazi, Y. Zou, D. Corzo, A. Basu, C. Ma, S. Dey, M. L. Tietze, U. Buttner, X. Wang, Z. Wang, M. N. Hedhili, C. Guo, T. Wu and A. Amassian, *Nat. Commun.*, 2018, **9**, 5354.

16 S. Albrecht and B. Rech, *Nat. Energy*, 2017, **2**, 16196.

17 T. He, S. Li, Y. Jiang, C. Qin, M. Cui, L. Qiao, H. Xu, J. Yang, R. Long, H. Wang and M. Yuan, *Nat. Commun.*, 2020, **11**, 1672.

18 G. Grancini and M. K. Nazeeruddin, *Nat. Rev. Mater.*, 2019, **4**, 4–22.

19 B. Náfrádi, P. Szirmai, M. Spina, H. Lee, O. V. Yazyev, A. Arakcheeva, D. Chernyshov, M. Gibert, L. Forró and E. Horváth, *Nat. Commun.*, 2016, **7**, 13406.

20 P. Daniel, A. Bulou, M. Rousseau, J. Nouet and M. Leblanc, *Phys. Rev. B: Condens. Matter Mater. Phys.*, 1990, **42**, 10545–10552.

21 P. J. Chupas, S. Chaudhuri, J. C. Hanson, X. Qiu, P. L. Lee, S. D. Shastri, S. J. L. Billinge and C. P. Grey, *J. Am. Chem. Soc.*, 2004, **126**, 4756–4757.

22 S. Ehsan, A. Tröster, F. Tran and P. Blaha, *Phys. Rev. Mater.*, 2018, **2**, 093610.

23 A. Marronnier, H. Lee, B. Geffroy, J. Even, Y. Bonnassieux and G. Roma, *J. Phys. Chem. Lett.*, 2017, **8**, 2659–2665.

24 W. Zhou, F. Sui, G. Zhong, G. Cheng, M. Pan, C. Yang and S. Ruan, *J. Phys. Chem. Lett.*, 2018, **9**, 4915–4920.

25 R. X. Yang, J. M. Skelton, E. L. da Silva, J. M. Frost and A. Walsh, *J. Phys. Chem. Lett.*, 2017, **8**, 4720–4726.

26 O. Yaffe, Y. Guo, L. Z. Tan, D. A. Egger, T. Hull, C. C. Stoumpos, F. Zheng, T. F. Heinz, L. Kronik, M. G. Kanatzidis, J. S. Owen, A. M. Rappe, M. A. Pimenta and L. E. Brus, *Phys. Rev. Lett.*, 2017, **118**, 136001.

27 M. Bianchini, J. Wang, R. J. Clément, B. Ouyang, P. Xiao, D. Kitchaev, T. Shi, Y. Zhang, Y. Wang, H. Kim, M. Zhang, J. Bai, F. Wang, W. Sun and G. Ceder, *Nat. Mater.*, 2020, **19**, 1088–1095.

28 L. Protesescu, S. Yakunin, M. I. Bodnarchuk, F. Krieg, R. Caputo, C. H. Hendon, R. X. Yang, A. Walsh and M. V. Kovalenko, *Nano Lett.*, 2015, **15**, 3692–3696.

29 S. Chaudhuri, P. Chupas, B. J. Morgan, P. A. Madden and C. P. Grey, *Phys. Chem. Chem. Phys.*, 2006, **8**, 5045–5055.

30 J. Chen, Y. Fu, L. Samad, L. Dang, Y. Zhao, S. Shen, L. Guo and S. Jin, *Nano Lett.*, 2017, **17**, 460–466.

31 K. Chen, W. Jin, Y. Zhang, T. Yang, P. Reiss, Q. Zhong, U. Bach, Q. Li, Y. Wang, H. Zhang, Q. Bao and Y. Liu, *J. Am. Chem. Soc.*, 2020, **142**, 3775–3783.

32 D. A. Egger, A. Bera, D. Cahen, G. Hodes, T. Kirchartz, L. Kronik, R. Lovrincic, A. M. Rappe, D. R. Reichman and O. Yaffe, *Adv. Mater.*, 2018, **30**, 1800691.

33 M. G. Goesten and R. Hoffmann, *J. Am. Chem. Soc.*, 2018, **140**, 12996–13010.

34 P. Giannozzi, S. Baroni, N. Bonini, M. Calandra, R. Car, C. Cavazzoni, D. Ceresoli, G. L. Chiarotti, M. Cococcioni, I. Dabo, A. Dal Corso, S. de Gironcoli, S. Fabris, G. Fratesi, R. Gebauer, U. Gerstmann, C. Gougoussis, A. Kokalj, M. Lazzeri, L. Martin-Samos, N. Marzari, F. Mauri, R. Mazzarello, S. Paolini, A. Pasquarello, L. Paulatto, C. Sbraccia, S. Scandolo, G. Sclauzero, A. P. Seitsonen, A. Smogunov, P. Umari and R. M. Wentzcovitch, *J. Phys.: Condens. Matter*, 2009, **21**, 395502.

35 G. Kresse and D. Joubert, *Phys. Rev. B: Condens. Matter Mater. Phys.*, 1999, **59**, 1758–1775.

36 J. P. Perdew, J. A. Chevary, S. H. Vosko, K. A. Jackson, M. R. Pederson, D. J. Singh and C. Fiolhais, *Phys. Rev. B: Condens. Matter Mater. Phys.*, 1992, **46**, 6671–6687.

37 S. L. Dudarev, G. A. Botton, S. Y. Savrasov, C. J. Humphreys and A. P. Sutton, *Phys. Rev. B: Condens. Matter Mater. Phys.*, 1998, **57**, 1505–1509.

38 R. F. Li, S. Q. Wu, Y. Yang and Z. Z. Zhu, *J. Phys. Chem. C*, 2010, **114**, 16813–16817.

39 A. D. Becke and E. R. Johnson, *J. Chem. Phys.*, 2007, **127**, 154108.

40 A. Otero-de-la-Roza and E. R. Johnson, *J. Chem. Phys.*, 2012, **136**, 174109.

41 M. Leblanc, R. De Pape, G. Ferey and J. Pannetier, *Solid State Commun.*, 1986, **58**, 171–176.

42 S. Baroni, S. de Gironcoli, A. Dal Corso and P. Giannozzi, *Rev. Mod. Phys.*, 2001, **73**, 515–562.
43 A. Otero-de-la-Roza and V. Luaña, *Comput. Phys. Commun.*, 2011, **182**, 1708–1720.
44 A. Otero-de-la-Roza, D. Abbasi-Pérez and V. Luaña, *Comput. Phys. Commun.*, 2011, **182**, 2232–2248.
45 P. Vinet, J. H. Rose, J. Ferrante and J. R. Smith, *World J. Condens. Matter Phys.*, 1989, **1**, 1941–1963.
46 F. Zhu, X. Lai, X. Wu, Y. Li and S. Qin, *Acta Crystallogr., Sect. B: Struct. Sci., Cryst. Eng. Mater.*, 2014, **70**, 801–808.
47 C. Lind, *Materials*, 2012, **5**, 1125–1154.
48 S. K. Kurtz, J. R. Hardy and J. W. Flocken, *Ferroelectrics*, 1988, **87**, 29–40.
49 R. X. Yang, J. M. Skelton, E. L. da Silva, J. M. Frost and A. Walsh, *J. Chem. Phys.*, 2020, **152**, 024703.
50 R. De Pape and G. Ferey, *Mater. Res. Bull.*, 1986, **21**, 971–978.
51 W. J. Croft and M. Kestigian, *J. Electrochem. Soc.*, 1968, **115**, 674.
52 M. A. Carpenter, A. I. Becerro and F. Seifert, *Am. Mineral.*, 2001, **86**, 348–363.
53 P. Daniel, A. Bulou, M. Rousseau, J. Nouet, J. L. Fourquet, M. Leblanc and R. Burriel, *World J. Condens. Matter Phys.*, 1990, **2**, 5663–5677.
54 C. Quarti, E. Mosconi, J. M. Ball, V. D'Innocenzo, C. Tao, S. Pathak, H. J. Snaith, A. Petrozza and F. De Angelis, *Energy Environ. Sci.*, 2016, **9**, 155–163.
55 F. Bertolotti, L. Protesescu, M. V. Kovalenko, S. Yakunin, A. Cervellino, S. J. L. Billinge, M. W. Terban, J. S. Pedersen, N. Masciocchi and A. Guagliardi, *ACS Nano*, 2017, **11**, 3819–3831.

Dear Author

Please use this PDF proof to check the layout of your article. If you would like any changes to be made to the layout, you can leave instructions in the online proofing interface. First, return to the online proofing interface by clicking "Edit" at the top page, then insert a Comment in the relevant location. Making your changes directly in the online proofing interface is the quickest, easiest way to correct and submit your proof.

Please note that changes made to the article in the online proofing interface will be added to the article before publication, but are not reflected in this PDF proof.